Manipulating light transmission and absorption via an achromatic reflectionless metasurface

Xiaoying Zheng[1†], Jing Lin[1*†], Zhuo Wang[1], Haoyang Zhou[1], Qiong He[1,2,3*] and Lei Zhou[1,2,3*]

[†]Xiaoying Zheng and Jing Lin contributed equally to this work.

*Correspondence:
jing_lin@fudan.edu.cn;
qionghe@fudan.edu.cn;
phzhou@fudan.edu.cn

[1] State Key Laboratory of Surface Physics, Key Laboratory of Micro and Nano Photonic Structures (Ministry of Education) and Department of Physics, Fudan University, 200433 Shanghai, People's Republic of China
[2] Academy for Engineering and Technology, Fudan University, 200433 Shanghai, People's Republic of China
[3] Collaborative Innovation Center of Advanced Microstructures, 210093 Nanjing, People's Republic of China

Abstract

Freely switching light transmission and absorption via an achromatic reflectionless screen is highly desired for many photonic applications (e.g., energy-harvesting, cloaking, etc.), but available meta-devices often exhibit reflections out of their narrow working bands. Here, we rigorously demonstrate that an optical metasurface formed by two resonator arrays coupled vertically can be perfectly reflectionless at all frequencies below the first diffraction mode, when the near-field (NF) and far-field (FF) couplings between two constitutional resonators satisfy certain conditions. Tuning intrinsic loss of the system can further modulate the ratio between light transmission and absorption, yet keeping reflection diminished strictly. Designing/fabricating a series of metasurfaces with different inter-resonator configurations, we experimentally illustrate how varying inter-resonator NF and FF couplings can drive the system to transit between different phase regions in a generic phase diagram. In particular, we experimentally demonstrate that a realistic metasurface satisfying the discovered criteria exhibits the desired achromatic reflectionless property within 160–220 THz (0–225 THz in simulation), yet behaving as a perfect absorber at ~ 203 THz. Our findings pave the road to realize meta-devices exhibiting designable transmission/absorption spectra immune from reflections, which may find many applications in practice.

Keywords: Metasurfaces, Couplings, Coupled-mode theory, Kerker condition, Perfect absorber

Introduction

Freely controlling transmission, reflection, and absorption of light wave through a thin screen is highly desired in photonics [1–6]. For instance, while perfect absorption is favored in energy harvesting, perfect transmission is desired in applications related to sensing and cloaking. In many scenarios, reflection is undesired as it can cause efficiency reduction and failure of the expected functionality (say, cloaking). Unfortunately, switching between perfect light transmission and perfect absorption is extremely challenging in thin-screen systems where energy transports in different channels are usually coupled in a complex way.

Metasurfaces, ultrathin metamaterials composed by subwavelength microstructures exhibiting tailored electromagnetic (EM) responses, offer a new platform to control light waves [7–11]. Many fascinating effects were realized based on metasurfaces, including perfect absorption [12–16], perfect transparency [17–21], and many others [22–28]. However, strong reflections always appear in such meta-devices at frequencies out of their narrow working bands in which perfect absorption/transparency is achieved. Recently, A few attempts appear to construct reflectionless metasurfaces based on different approaches such as antireflection coating [29, 30], anomalous Brewster effect [31, 32], specular reflection reduction [33], etc. One typical design approach is to put into a unit cell two resonators, exhibiting electric and magnetic responses, respectively, so that their back scatterings can exactly cancel each other under certain condition (e.g., the Kerker condition [34–37]). However, since two created resonance modes usually exhibit distinct frequency dispersions, in most cases the Kerker condition is satisfied only at a single frequency, making the constructed metasurfaces exhibiting narrow working bands [6, 38–41]. Despite of many efforts devoted to expanding the reflectionless bandwidths through structural optimizations [32, 33, 42–45], such an issue remains intrinsic, and new mechanism is highly desired for designing achromatic reflectionless metasurfaces.

In this work, we propose a new strategy to realize achromatic reflectionless metasurfaces (see Fig. 1). Distinct from metasurfaces consisting of resonators placed on the same plane [46–49], here we study a bi-layer system containing two arrays of resonators placed on different planes. The inter-layer distance is a new parameter to tune both NF and FF couplings between two resonators (see inset in Fig. 1), which is lacked in previously studied systems. Base on coupled-mode-theory (CMT) calculations, we first establish a generic phase diagram showing how the reflection property of such system varies against the inter-resonator NF and FF couplings. We find that the Kerker condition can
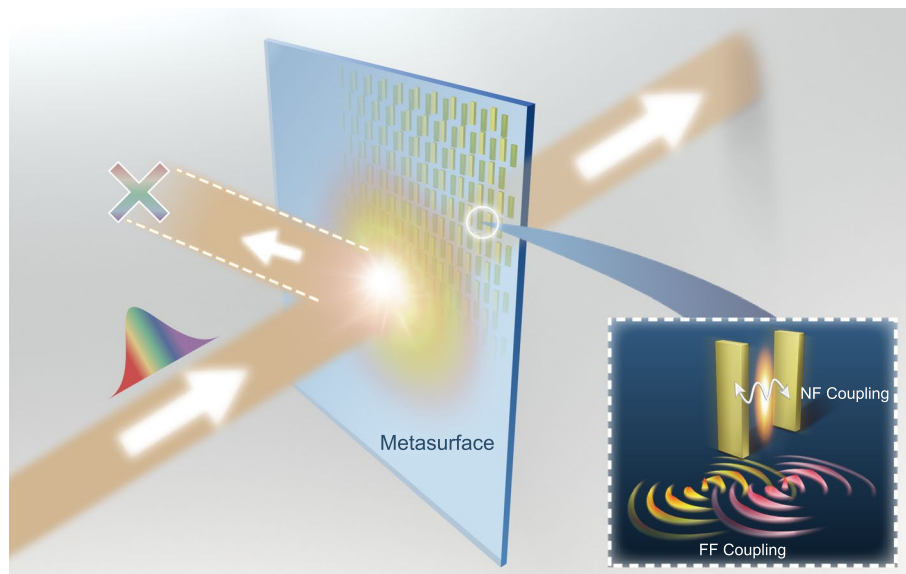

Fig. 1 Schematics of the achromatic reflectionless bi-layer metasurface. Tailoring near-field and far-field couplings between two optically identical resonators placed on different phase planes (inset), one can realize a metasurface that is immune from reflections at all frequencies below the first diffraction mode, yet with light power switched between transmission and absorption channels dictated by the intrinsic loss

be rigorously satisfied at all frequencies below the first diffraction mode, as long as the NF and FF coupling strengths between two resonators meet a set of conditions. Moreover, adding Ohmic losses to the system does not violate the Kerker condition, but rather efficiently re-allocate light power between transmission and absorption channels. We design/fabricate a series of bi-layer metasurfaces and experimentally illustrate how varying their geometric configurations can drive them move inside the phase diagram via modulating two coupling strengths. We finally realize a metasurface satisfying the Kerker criterion, and experimentally demonstrate that it exhibits perfect absorption around 203 THz within an ultra-wideband reflectionless frequency band (160–220 THz in experiment, 0–225 THz in simulation). Many applications can be expected based on our reflectionless platform, with a tunable absorber numerically demonstrated as a particular example.

Results and discussion

Generic phase diagram of the bi-layer systems

We establish a phase diagram for the proposed bi-layer systems based on CMT analyses [49–51]. In our system, two layers of our system are both periodic arrays with subwavelength spacing, such that only the zero-order mode of transmission/reflection can survive. As depicted in the inset to Fig. 2a, the bi-layer system can be generically described by a 2-mode 2-port model, with time evolutions of the amplitudes $a_{i=1,2}$ of two resonance modes satisfying the following equations:

$$
\begin{cases}
\frac{1}{2\pi}\frac{\partial}{\partial t}\begin{pmatrix} a_1 \\ a_2 \end{pmatrix} = -i\begin{pmatrix} f_0 & \kappa \\ \kappa & f_0 \end{pmatrix}\begin{pmatrix} a_1 \\ a_2 \end{pmatrix} + \begin{pmatrix} -\Gamma_r - \Gamma_i & X \\ X & -\Gamma_r - \Gamma_i \end{pmatrix}\begin{pmatrix} a_1 \\ a_2 \end{pmatrix} + \begin{pmatrix} d_{11} \\ d_{12} \end{pmatrix}s_1^+ \\
\begin{pmatrix} s_1^- \\ s_2^- \end{pmatrix} = \mathbf{C}\begin{pmatrix} s_1^+ \\ s_2^+ \end{pmatrix} + \begin{pmatrix} d_{11} & d_{12} \\ d_{21} & d_{22} \end{pmatrix}\begin{pmatrix} a_1 \\ a_2 \end{pmatrix}
\end{cases}.
$$

$$(1)$$

Here, we assume that the two modes are identical, with f_0, Γ_r and Γ_i describing their resonant frequencies, radiation and absorption damping, respectively. Meanwhile, κ and X represent NF and FF couplings between two modes, d_{ji} describes the coupling between the j-th external port and the i-th excited mode, and $s_j^{+(-)}$ denotes the amplitudes of incoming (out-going) waves from (to) the j-th port. $\mathbf{C} = \begin{pmatrix} r_0 & t_0 \\ t_0 & -r_0 \end{pmatrix}$ denotes the scattering properties of the background which is set as vacuum at the moment (i.e. $r_0 = 0$ and $t_0 = 1$). According to energy conservation and time reversal symmetry, we prove that $d_{11} = d_{21} = i\sqrt{\Gamma_r}$, $d_{12} = i\sqrt{\Gamma_r}\exp(i\theta_X)$ and $d_{22} = i\sqrt{\Gamma_r}\exp(-i\theta_X)$, where θ_X measures the phase difference between radiated far fields from two excited resonators (see Fig. 2a). Finally, we find that the FF inter-resonator coupling X is not an independent parameter, but can be expressed as $X = -\Gamma_r\exp(i\theta_X)$ [49]. All derivation details can be found in Section 1 of Supplementary Information (SI). In what follows, we consider the lossless case (i.e. $\Gamma_i = 0$) first, where only four independent parameters (f_0, Γ_r, κ and θ_X) are relevant. We note that all these parameters are assumed as frequency-independent constants in CMT [49–51] derived under the high-Q approximation.

Equation (1) can be analytically solved through standard CMT analyses. The identical symmetry possessed by two matrixes in the first line of Eq. (1) ensures
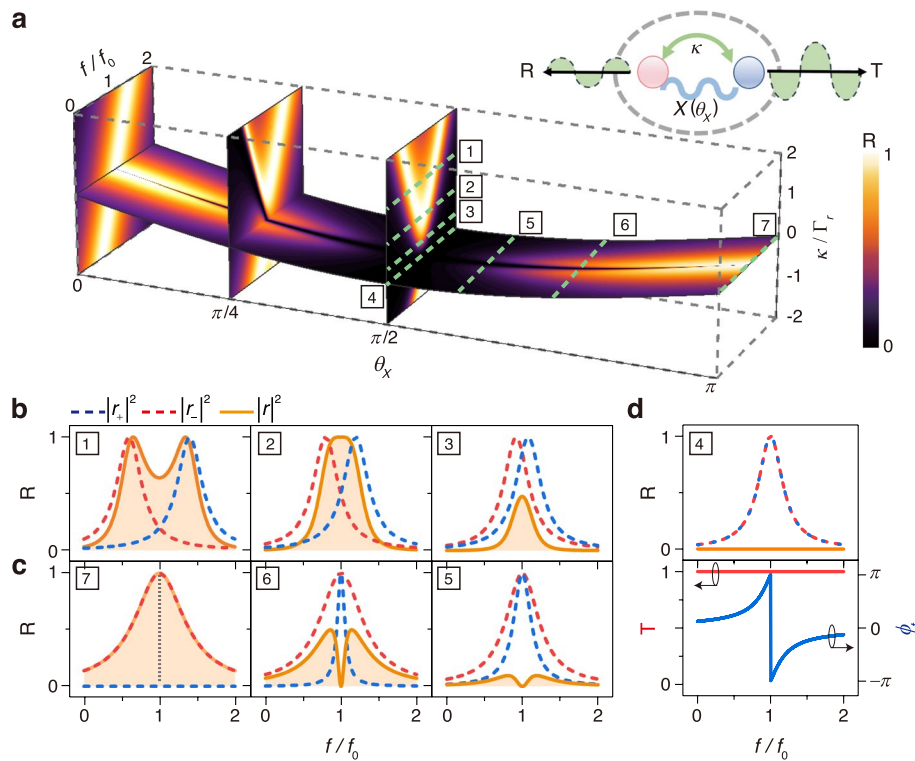
Fig. 2 Generic phase diagram for the bi-layer metasurfaces. **a** Reflectance of the 2-mode 2-port model (inset) calculated by Eq. (3) in the main text, as a function of frequency, θ_X and κ, with $\kappa - \text{Im}(X) = 0$ satisfied on the horizontal curved surface. Green dash lines labeled with #1 to #4 represent the cases of $\kappa/\Gamma_r = 1$, $0, -0.6, -1$ with fixed $\theta_X = \pi/2$, while those labeled with #4 to #7 represent the cases of $\theta_X = \pi/2, 3\pi/5, 3\pi/4$, π with $\kappa - \text{Im}(X) = 0$ satisfied, respectively. Here, $\Gamma_r/f_0 = 0.2$. **b-c** Calculated reflection spectra $|r|^2$ and those contributed by two decoupled modes $|r_\pm|^2$ calculated by Eq. (3) for 6 systems corresponding to 6 dashed lines shown in **a**. **d** Upper panel: spectra of $|r|^2$ and $|r_\pm|^2$ calculated by Eq. (3) for the #4 system; Lower panel: computed spectra of transmittance and transmission phase for the #4 system

that they can be simultaneously diagonalized with an orthogonal transformation $\tilde{a}_\pm = (a_2 \pm a_1)/\sqrt{2}$. After the transformation, we get two decoupled hybridized modes with

$$\tilde{f}_\pm = f_0 \pm (\kappa + \Gamma_r \sin\theta_X), \quad \tilde{\Gamma}_\pm = \Gamma_r(1 \pm \cos\theta_X) \tag{2}$$

being their resonant frequencies and radiation damping, respectively. We note from Eq. (2) that the shift in frequency is determined by the NF coupling κ and the Hermitian part of FF coupling $\text{Im}(X)$, while the shift in radiation damping is solely dictated by the non-Hermitian part of FF coupling $\text{Re}(X)$. Reflection coefficient of our metasurface can then be analytically derived as (see Sec. 1 in SI)

$$r = r_+ + r_-, r_+ = \frac{-\Gamma_r}{2}\frac{\left(1 + e^{i\theta_X}\right)^2}{-i\left(f - \tilde{f}_+\right) + \tilde{\Gamma}_+}, r_- = \frac{-\Gamma_r}{2}\frac{\left(1 - e^{i\theta_X}\right)^2}{-i\left(f - \tilde{f}_-\right) + \tilde{\Gamma}_-}, \tag{3}$$

where r_+ and r_- denote the scatterings due to two independent modes.

We employ Eq. (3) to study how the reflectance $R = |r|^2$ varies against κ and θ_X with all single-mode properties (f_0 and Γ_r) fixed. Fixing θ_X at 0, $\pi/4$ and $\pi/2$, respectively,

we illustrate on three vertical planes in Fig. 2a how the obtained reflectance spectrum $R(f)$ changes versus κ. While two branches of reflection peaks appear on the planes at $\pi/4$ and $\pi/2$, only one branch exists on the plane at $\theta_X = 0$ since one mode becomes completely dark ($\tilde{\Gamma}_- = 0$) dictated by the symmetry, which is also called a bound state in continuum [36, 52]. Set κ as 3 different values on the $\theta_X = \pi/2$ plane, we depict in Fig. 2b the calculated reflection spectra $R(f)$ (solid lines) and those contributed by two decoupled modes $|r_{\pm}(f)|^2$ as defined in Eq. (3) (dotted lines). We find that varying κ modifies two peak positions keeping the bandwidths of two decoupled modes unchanged, in consistency with Eq. (2). The final reflection spectrum $R(f)$ is thus significantly modulated by κ due to the interference between two modes (See Fig. S2 for more details in Sec. 2 of SI). Meanwhile, Eq. (2) predicts that the two hybridized modes exhibit identical resonance frequencies in the cases of $\kappa = -\Gamma_r \sin \theta_X$, corresponding to a curved surface in Fig. 2. Choosing three typical cases on the curved surface, we depict in Fig. 2c how changing θ_X further modulates the final reflection spectrum. As shown in Fig. 2c, now the R spectrum is an interference of two degenerate modes exhibiting different radiation damping, in consistency with Eq. (2). In particular, in the case of $\theta_X = \pi/2$ (the #4 line in Fig. 2a), the two degenerate modes are out of phase and of identical bandwidths, and therefore, their interference leads to complete cancellation of reflections within the entire considered frequency range as shown in Fig. 2d (i.e., $R(f) \equiv 0$). Meanwhile, it is noticeable that the transmission phase covers a whole 2π range. Such a rigorous zero-reflection solution can be rephrased as the following condition

$$|X - i\kappa| = |-\Gamma_r \cos \theta_X - i(\kappa + \Gamma_r \sin \theta_X)| = 0 \tag{4}$$

which states that the total effective coupling (including both Hermitian and non-Hermitian parts) that we define as $\xi = |X - i\kappa|$ between two original modes must be exactly zero.

We now discuss the role played by the absorption loss. Figure 3a and b depict, respectively, the calculated reflectance R on two $\theta_X - f$ planes (with $\kappa = -\Gamma_r \sin \theta_X$ fixed) and two $\kappa - f$ planes (with $\theta_X = \pi/2$ fixed) with different absorption damping parameters ($\Gamma_i = 0$ and $\Gamma_i = 0.5\,\Gamma_r$). Obviously, absorption loss does not affect the desired zero-reflection property of the system, as long as Eq. (4) is met (dashed lines in Fig. 3a-b, more cases are presented in Figs. S3-S4 of SI). In fact, turning on Γ_i in Eq. (1) does not violate the symmetry possessed by our system, and thus reflections from two decoupled modes still exactly cancel each other. Rigorously solving Eq. (1) with Γ_i present, we get the following analytical expressions (see Sec. 1 in SI for detailed derivations):

$$r = 0; \quad t = 1 - \frac{2\Gamma_r}{-i(f - f_0) + \Gamma_r + \Gamma_i}. \tag{5}$$

Remarkably, we find that the expression of t is exactly the same as that of the reflection co-efficient of a 1-port 1-mode model, widely used to describe the metal/insulator/metal (MIM) system [13]. Therefore, all interesting physical behaviors revealed in the MIM systems are also expected here [13]. Indeed, increasing Γ_i can gradually enhance the absorbance A until the critical-damping condition ($\Gamma_i = \Gamma_r$) is reached at which
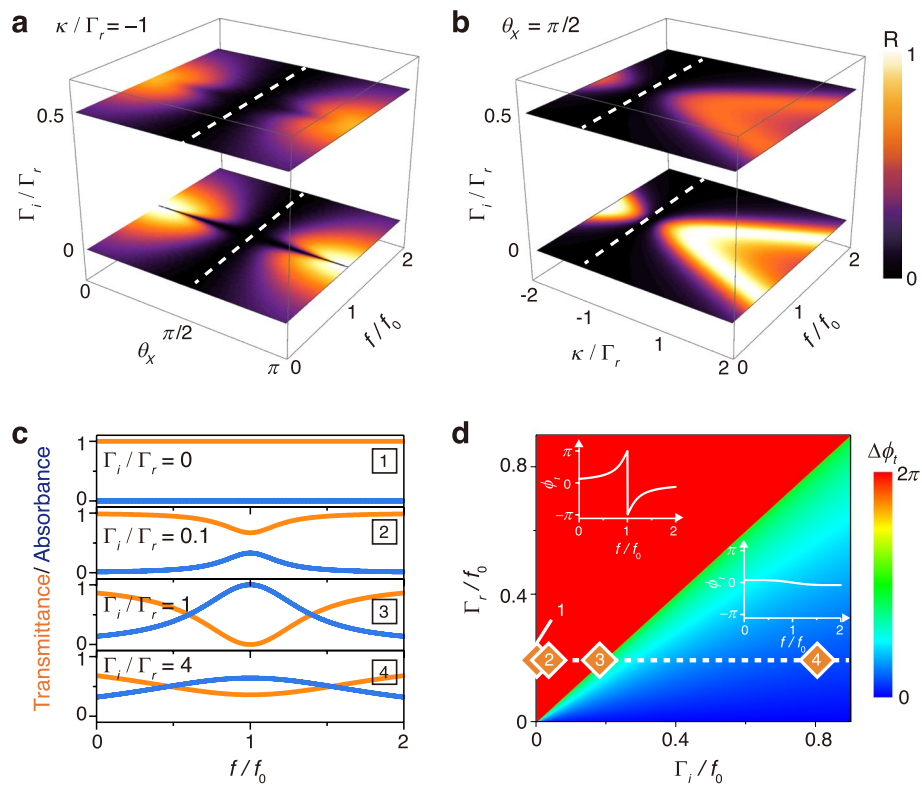
Fig. 3 Influences of Γ_i on the optical properties of the model satisfying Eq. (4). **a** Reflectance of the model system versus frequency and θ_χ in the cases of $\Gamma_i/\Gamma_r = 0$ and $\Gamma_i/\Gamma_r = 0.5$, respectively, with κ/Γ_r fixed as -1. **b** Reflectance of the model system versus frequency and κ/Γ_r, in the cases of $\Gamma_i/\Gamma_r = 0$ and $\Gamma_i/\Gamma_r = 0.5$, respectively, with θ_χ fixed as $\pi/2$. **c** Calculated spectra of transmittance (orange lines) and absorbance (blue lines) of the model systems with $\kappa/\Gamma_r = -1$ and $\theta_\chi = \pi/2$, and with Γ_i/Γ_r taking 4 different values. **d** Transmission phase coverage of the model system versus Γ_i/f_0 and Γ_r/f_0. Four symbols labeled with #1–4 correspond four cases studied in **c**. Upper and lower insets depict the calculated spectra of transmission phase for the systems labeled with #1 and #4, respectively. In all cases studied, we have $\Gamma_r/f_0 = 0.2$

perfect absorption happens ($A(f_0) = 1$), while further increasing Γ_i in the region of $\Gamma_i > \Gamma_r$ will decrease the absorbance (see blue lines in Fig. 3c). Along varying Γ_i, however, we find distinct behaviors exhibited by the transmission phase $\phi_t(f) = \arg[t(f)]$ in two different cases with $\Gamma_i < \Gamma_r$ and $\Gamma_i > \Gamma_r$, respectively (see insets to Fig. 3d). Color map in Fig. 3d depicts the variation range $\Delta\phi_t$ of transmission phase $\phi_t(f)$ upon frequency changing, as the functions of Γ_i and Γ_r. The critical-damping line ($\Gamma_i = \Gamma_r$) separates the whole $\Gamma_i - \Gamma_r$ phase diagram into two parts, which are the under-damped region ($\Gamma_i < \Gamma_r$) with $\Delta\phi_t$ covering a whole 2π range and the over-damped region ($\Gamma_i > \Gamma_r$) with $\Delta\phi_t$ less than π. In all these cases studied, we have $A(f) + T(f) = 1$ strictly satisfied (see Fig. 3c), since the reflection channel of our system is completely blocked as long as Eq. (4) is satisfied. Therefore, tuning Γ_i in our system can efficiently re-allocate the power of light between transmission and absorption channels, in an ideal achromatic reflectionless platform.

Experimental demonstration of the phase diagram

We now experimentally realize a series of bi-layer metasurfaces exhibiting different NF and FF couplings, starting from designing two optical modes exhibiting identical resonance frequency f_0 and radiation damping Γ_r. Since in reality it is still challenging

to fabricate a free-standing sample with two resonators on two sides of a thin dielectric spacer, here we choose to design our bi-layer metasurface in such a configuration that one plasmonic resonator (an Au bar) is on top of a SiO_2 substrate while another Au bar is buried inside the substrate (see Fig. 4a). As the two resonators are now in different dielectric environments, they must possess different geometries in order to exhibit identical optical responses. Moreover, the presence of a dielectric substrate changes the background scattering matrix **C** and the coupling matrix d_{ji} in Eq. (1). Despite of these differences with the ideal case, we still analytically proved the following two conclusions for such metasurfaces (see Sec. 3 in SI): 1) as the Kerker condition (Eq. (4)) is met, such a metasurface in the lossless condition only exhibits the
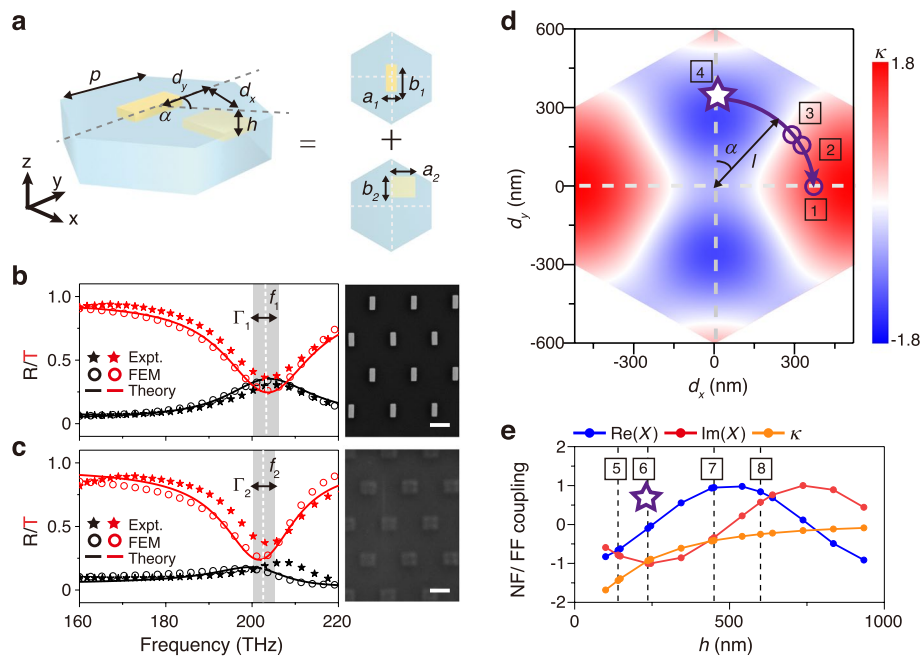

Fig. 4 Optical properties of two basic resonators and their NF and FF couplings. **a** A unit cell of the bi-layer metasurface containing one Au nano bar on top of a SiO_2 substrate and another Au nano bar buried inside the substrate at a depth *h*. Here the two resonators are of the same thickness (30 nm) and different lateral sizes, with their centers on different lateral positions on the *xy*-plane. **b** Spectra of reflectance/transmittance of the metasurface containing top resonators (with $a_1 = 140$ nm and $b_1 = 340$ nm) arranged in a hexagonal lattice with periodicity $p = 600$ nm, obtained by experiments (stars), simulations (circles) and CMT calculations (solid lines) with parameters computed by the LEM theory ($f_1 = 203.32$ THz, $\Gamma_{1r} = 5.997$ THz, $\Gamma_{1i} = 6.140$ THz). **c** Spectra of reflectance/ transmittance of the metasurface containing resonators (with $a_2 = 320$ nm and $b_2 = 280$ nm) buried inside the substrate at $h = 236$ nm arranged in a hexagonal lattice with periodicity $p = 600$ nm, obtained by experiments (stars), simulations (circles) and CMT calculations (solid lines) with parameters computed by the LEM theory ($f_2 = 202.57$ THz, $\Gamma_{2r} = 4.985$ THz, $\Gamma_{2i} = 4.975$ THz). White dashed lines and gray areas in **b**-**c** denote the frequencies and radiation damping of the resonant modes, calculated by LEM theory, and right panels in **b**-**c** are the SEM images of the fabricated samples with scale bars (white lines) of 500 nm. **d** LEM-calculated near-field coupling κ between two resonators versus their relative lateral configuration (d_x, d_y) with fixed vertical distance $h = 236$ nm. Points labeled with 1–4 represent the cases with $a = 90°, 65°, 55°, 0°$ on the circle $l = \sqrt{d_x^2 + d_y^2} = 345$ nm. **e** LEM-calculated inter-resonator couplings (*X* and κ) as functions of *h*, with fixed $a = 0°$ and $l = \sqrt{d_x^2 + d_y^2} = 345$ nm. Dashed lines labeled with #5–8 represent the cases with $h = 140, 236, 450, 600$ nm, respectively. The violet star represents the position of critical point with $\kappa - \text{Im}(X) = 0$ and $\theta_X = \pi/2$ satisfied. Here, κ and *X* are scaled by $\sqrt{\Gamma_{1r}\Gamma_{2r}}$, and the SiO_2 substrate has a thickness of 500 μm in experiments and is treated as a semi-infinite medium in simulations

background reflectance within the entire frequency band below the first diffraction mode; 2) perfect absorption can still happen as the critical damping condition is met.

We fix the geometric structures of two basic resonators with the help of finite-element-method (FEM) simulations, and fabricate two single-layer metasurfaces according to our designs using the standard electron-beam lithography (EBL) method. As shown in the right panels of Fig. 4b-c, each metasurface contains resonators of one type arranged in a hexagonal lattice with periodicity 600 nm, while resonators in the second sample are buried inside the substrate at the depth $h = 236$ nm [53]. Illuminating two samples with y-polarized normally incident light, we experimentally measure their scattering spectra, with reference signals taken as those obtained with the sample replaced by a gold mirror (for reflection) and the quartz substrate (for transmission), respectively (Sec. 4 in SI). Figure 4b-c clearly show that the two systems exhibit nearly identical measured transmission/reflection spectra (stars), which are in good agreement with their corresponding FEM simulations (circles). We further employ a recently developed leaky-eigen-mode (LEM) theory [49] to directly compute the optical characteristics (i.e., f_0, Γ_r and Γ_i) of the resonance modes supported by two systems, based on their LEM wave-functions derived from Maxwell equations (see more details in Sec. 5 of SI). Put these LEM-computed parameters into the CMT, we obtain the reflection spectra of two metasurfaces (solid lines in Fig. 4b-c), which are in excellent agreement with simulation and experimental results.

With LEM wave-functions of two designed resonance modes known, we can employ them to directly compute the FF and NF coupling parameters (e.g., κ and X) between two resonators, which are arranged in different relative configurations in forming our bi-layer metasurfaces. Obviously, while the inter-layer distance h dictates the FF coupling, the lateral relative configuration between two resonators and h are collectively responsible for the NF coupling. Figure 4e depicts how the LEM-computed X and κ changes as a function of h with lateral positions of two bars fixed. We find both $\text{Re}(X)$ and $\text{Im}(X)$ vary periodically versus h, as expected, while κ decays as h increase since near field localize around the particles. In particular, we get $\text{Re}(X) = 0$ at $h = 236$ nm, which is very close to the prediction $h = \lambda_n/4$ (with $\lambda_n = 985$ nm being the resonance wavelength inside the dielectric substrate). The slight discrepancy is caused by the difference between the realistic structures and the ideal model. Fix the top bar at the unit-cell enter $(0,0)$ and put the second bar at (d_x, d_y) on the $h = 236$ nm plane, we employ the LEM-theory to calculate how κ varies against d_x and d_y, and depict the results as a color map in Fig. 4d. In particular, we find that κ can continuously change from a negative value to a positive one as the relative horizontal angle α between two bars varies from 0° to 90° (see the circle with radius $l = \sqrt{d_x^2 + d_y^2} = 345$ nm in Fig. 4d). These results suggest that we have enough tuning freedoms to design bi-layer metasurfaces exhibiting different κ and X, and in turn, different optical responses.

We choose 7 points on the phase diagrams (see Fig. 4d-e) to design the corresponding metasurfaces. Samples #1–4 exhibit identical inter-layer distance h and different relative orientation angle α (Fig. 4d), while samples #5–8 have the same value of α but with h changing from 140 to 600 nm (Fig. 4e). We note that samples #4 and #6 are the same, although they are on different variation paths. To check whether these samples meet the Kerker condition Eq. (4), we depict the positions of 7 samples on the $\xi \sim \{\kappa, \theta_X\}$ phase
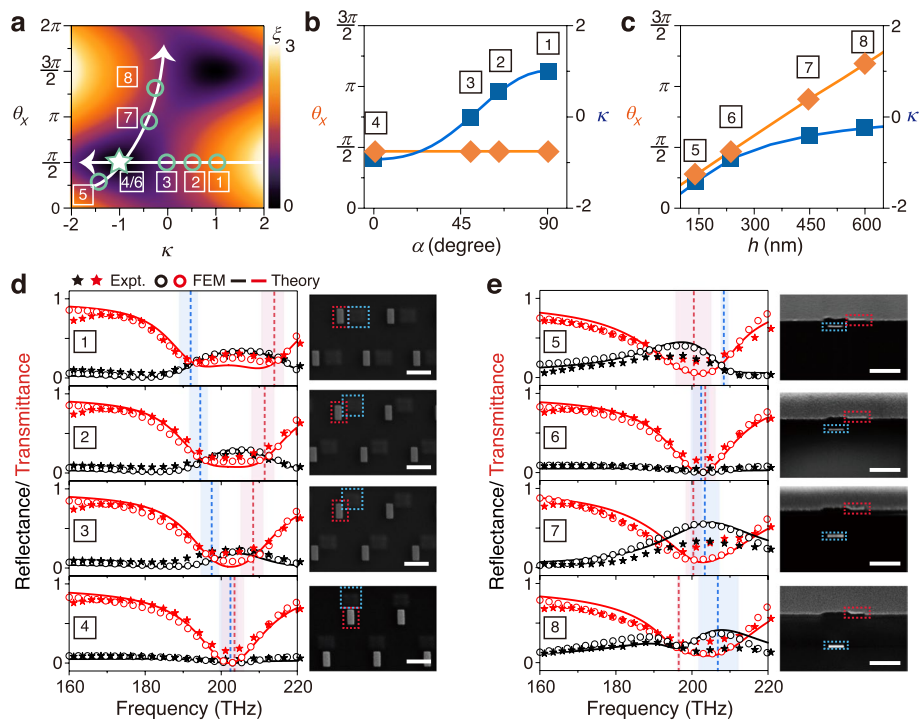
Fig. 5 Experimental characterizations on two series of metasurfaces with varying NF and FF couplings. **a** Calculated value of $\xi = |X - i\kappa|$ (color map) versus κ and θ_X, with points labeled with #1–8 representing those shown in Fig. 4d-e. **b-c** LEM-calculated κ and θ_X for two series of samples. **d** Spectra of reflectance/transmittance of samples #1–4 with top-view SEM pictures (scale bars: 500 nm) shown in the right panel, obtained by experiments (stars), simulations (circles) and CMT calculations (solid lines) with parameters computed by the LEM theory, respectively. Here the bumps in **d** marked by blue dotted lines are SiO_2 bumps stemming from the deposition process corresponding to the location of the bottom resonators. **e** Spectra of reflectance/transmittance of samples #5–8 with side-view FIB-SEM pictures (scale bars: 500 nm) shown in the right panel, obtained by experiments (stars), simulations (circles) and CMT calculations (solid lines) with parameters computed by the LEM theory, respectively. Dotted lines and shaded areas in **d-e** represent the resonance frequencies and radiation damping of the hybrid modes calculated with the LEM theory, respectively, while the dotted-line rectangles in the sample images denote the positions of two bars. Here, κ and X are scaled by $\sqrt{\Gamma_{1r}\Gamma_{2r}}$

diagram (Fig. 5a). We see clearly that sample #4 (the green star) just locates at the $\xi = 0$ point meeting the Kerker condition Eq. (4). We note that surface roughness caused by the presence of nano-structures in the bottom layer does not modify the EM responses of our metasurface obviously (See Fig. S9 in Sec.6 of SI).

We fabricate these bi-layer samples with a two-step EBL process (see Sec. 7 in SI) and experimentally characterize their optical properties. The top-view scanning-electron-microscopy (SEM) pictures of samples #1−4 (see right panel in Fig. 5d) show that two resonators are in different relative lateral configurations, while the side-view Focus-Ion-Beam (FIB) - SEM pictures of samples #5−8 (see right panel in Fig. 5e) reveal that two resonators exhibit different vertical distances h, in consistency with Fig. 4d-e. Shine these samples with y-polarized normally incident light, we measure their reflection and transmission spectra (stars in Fig. 5d-e), which are in excellent agreement with FEM simulations (see circles in Fig. 5d-e).

We first discuss the sample series #1−4. We find from experimental results (Fig. 5d) that decreasing α mainly changes the frequency interval between two reflection peaks,

but has negligible influences on their bandwidths. To understand the physics, we employ the LEM theory to compute (κ, θ_X) of samples #1–4. We find from Fig. 5b that these samples exhibit continuously varying κ and identical θ_X as α changes, which well explains the salient features revealed in the reflection spectra. Put the LEM-computed (κ, θ_X) into the CMT equations (see Sec. 3 in SI), we find that the CMT-calculated reflection spectra $R(f)$ (solid lines in Fig. 5d) are in excellent agreement with both simulation and experimental results. Obviously, such a line-shape evolution is governed by essentially the same physics as that discussed in Fig. 2b for the model systems.

We next discuss the sample series #5–8. We find from the measured spectra (Fig. 5e) that changing h in this series modifies not only the frequency positions but also the bandwidths of two modes. These features can be well explained by the LEM-calculated (κ, θ_X) as varying h (Fig. 5c). Again, put the LEM-computed values (κ, θ_X) in to the CMT equations, we find that the CMT-computed reflection spectra $R(f)$ (solid lines in Fig. 5e) are in good agreement with both numerical and measured results. Slight discrepancies between experimental and simulation results can be attributed to differences in material parameters in the double-layer metasurface and their single-layer counterparts, caused by fabrication imperfections. In particular, the calculated positions and bandwidths of two hybridized modes, labeled by the dashed lines and shaded areas in Fig. 5e, respectively, re-enforce our notion that changing h affects both the frequencies and bandwidths of the hybridized modes through modifying both NF and FF couplings between two resonators.

Achromatic reflectionless metasurface

We now focus on the sample #4 (or #6), corresponding to the case of $\xi = 0$ in Fig. 5a. Experimental results clearly show that the reflectance of this sample nearly maintains at the background value within the whole experimentally accessible frequency range (160 to 220 THz) except at the resonance frequency. In fact, simulation results indicate that the sample maintains at the background value in a frequency range (0–225THz) far beyond that experimentally accessible (Fig. 6b). We note that diffractions inevitably appear at frequencies above 225 THz, since the realistic metasurface is a periodic structure. We note that our metasurface is designed under normal incidence, and its achromatic reflectionless property is maintained only as the incident angle lies in a narrow range centered at 0°, which can be enlarged by structural optimizations. Achromatic reflectionless metasurfaces under oblique incidence are also designable, as long as the system still works below the first-order diffraction (see more details in Sec. 8 of SI).

We next study the absorption properties of the fabricated sample. Computing the absorption spectrum $A(f)$ using $A = 1 - R - T$, we find that the experimentally measured absorbance A reaches 96% at the resonance frequency 203.1 THz (Fig. 6b) at which the transmittance T approaches zero. At frequencies away from the resonance one, A diminishes and T increases but $A + T = 1$ maintains approximately. To understand the intrinsic physics, we employ the LEM theory to calculate the intrinsic damping parameters of two resonance modes (see Sec. 5 of SI), which confirms that the critical damping condition $(\Gamma_i = \Gamma_r)$ is indeed approximately satisfied for present system which already satisfies the Kerker condition Eq. (4).
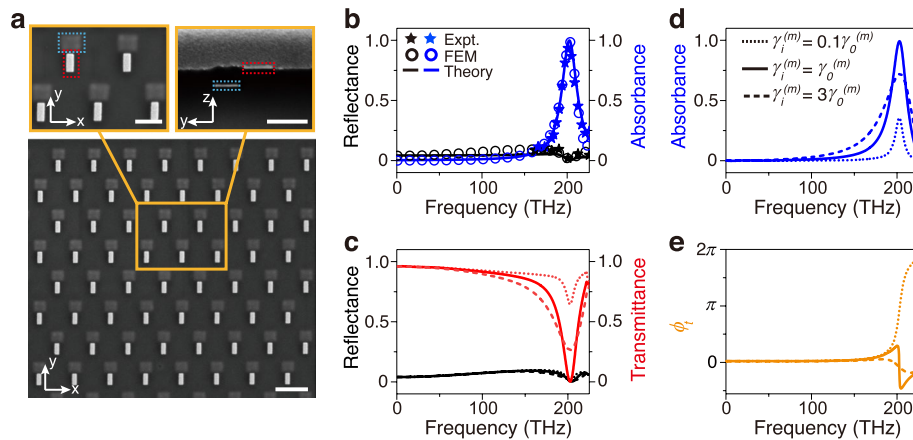
Fig. 6 Experimental/numerical characterizations on the achromatic reflectionless metasurface with tunable loss. **a** Top-view SEM image of sample #4 (scale bar: 1 μm) with top-left inset depicting a zoom-in top-view SEM picture (scale bar: 500 nm) and top-right inset depicting a side-view FIB-SEM picture (scale bar: 500 nm), respectively. **b** Spectra of reflectance and absorbance of sample #4 within the wide frequency range of 0–225 THz, obtained by experiments (stars), simulations (circles) and CMT calculations (solid lines) with parameters computed by the LEM theory, respectively. **c-e** FEM-simulated spectra of **c** reflectance/transmittance, **d** absorbance and **e** transmission phase for the sample #4, assuming that its absorption damping parameters $\gamma_i^{(m)}$ ($m=1,2$) take different values (The dotted/ solid/ dashed lines denote cases with $\gamma_i^{(m)} = 0.1\gamma_0^{(m)}$, $\gamma_i^{(m)} = \gamma_0^{(m)}$, and $\gamma_i^{(m)} = 3\gamma_0^{(m)}$, respectively). Here, $\gamma_0^{(1)} = 3.182 \times 10^{16} s^{-1}$ and $\gamma_0^{(2)} = 3.672 \times 10^{16} s^{-1}$ denote the absorption damping parameters adopted in our FEM simulations corresponding to the experimentally realized sample, obtained by fitting with the measured spectra in Fig. 4

Moreover, we find that tuning the intrinsic loss in this sample can further modulate the ratio between light transmission and absorption, yet keeping reflection diminished. To demonstrate this point, we perform a series of FEM simulations assuming that the damping parameter $\gamma_i^{(m)}$ ($m=1,2$) in the Drude model ($\varepsilon(\omega) = \varepsilon_\infty - \omega_p^2/\left(\omega^2 + i\omega\gamma_i^{(m)}\right)$) describing our plasmonic metals forming the m-th resonator ($m=1, 2$) take different values. Since the two metallic resonators are in different dielectric environments, it is quite natural to expect that $\gamma_i^{(1)} \neq \gamma_i^{(2)}$. As shown in Fig. 6d, tuning $\gamma_i^{(m)}$ from $0.1\gamma_0^{(m)}$ to $3\gamma_0^{(m)}$ with $\gamma_0^{(m)}$ representing the experimental case, we find that the peak absorbance A first increase from 36% to 100% and then decreases, in consistency with the under-damping to over-damping transition discussed in Sec. 2 (see Fig. 3). Meanwhile, the reflectance keeps negligible in all these cases studied (black lines in Fig. 6c), which is again consistent with the notion that the reflection channel is blocked under the Kerker condition (Eq. (4)). Finally, transmission phase spectra of the system with different $\gamma_i^{(m)}$ (Fig. 6e) also exhibit the under-damping to over-damping transition, in consistency with Fig. 3d. These results suggest the possibilities to realize transmission-mode tunable meta-devices for phase modulations and wave-front controls, through controlling the intrinsic damping of constitutional materials via electric or optical means.

Conclusion

To summarize, we employ CMT analyses to rigorously demonstrate that an optical metasurface formed by two arrays of resonators can be perfectly reflectionless at all frequencies below the first diffraction mode, when the NF and FF couplings between two constitutional resonators satisfy certain conditions. Tuning the intrinsic loss of the

system can further modulate the ratio between light transmission and absorption, yet keeping reflection diminished strictly. We design/fabricate a series of metasurfaces and experimentally illustrate how the reflection line-shape of such metasurface is tailored by inter-resonator NF and FF couplings. In particular, we identify a specific metasurface from the sample series and experimentally demonstrate that it is immune from reflections within an ultra-wide frequency range (experiment: 160–220 THz; simulations: 0–225 THz), yet behaving as a perfect absorber at ~ 203 THz.

Many future works can be stimulated from the present study. For example, realizing such reflectionless meta-devices can find immediate applications in sensing, cloaking, and energy harvesting. Moreover, modulating transmission phase of light via tuning the intrinsic loss in our meta-device (Fig. 6) can inspire tunable transmissive meta-devices for high-efficiency wave-front controls. Finally, realizing free-standing samples exhibiting background-free achromatic reflections in different frequency regimes are challenging and interesting future projects.

Methods

Simulations

All FEM simulations are performed with the commercial software COMSOL Multiphysics. Permittivity of Au is described by the Drude model $\varepsilon(\omega) = \varepsilon_\infty - \omega_p^2 / \left(\omega^2 + i\omega \gamma_i^{(m)} \right)$ with $\varepsilon_\infty = 9$ and $\omega_p = 1.367 \times 10^{16} s^{-1}$. The damping parameter is set as $\gamma_0^{(1)} = 3.182 \times 10^{16} s^{-1}$ for top resonators and as $\gamma_0^{(2)} = 3.672 \times 10^{16} s^{-1}$ for the resonators buried inside the substrate, obtained by fitting with our experimentally measured optical spectra for corresponding metasurfaces (Fig. 4). The SiO$_2$ substrate was considered as a lossless dielectric with permittivity $\varepsilon_{\mathrm{SiO}_2} = 2.25$. We note that additional losses caused by surface roughness, grain boundary effects, existence of adhesion layer as well as dielectric losses, have been effectively considered in choosing the values of two parameters $\gamma_0^{(m)} (m = 1, 2)$ describing the damping rates of Au forming two resonators.

Fabrications

All bi-layer samples were fabricated using two-step EBL and lift-off processes. First, the positive resist MMA EL6 (200 nm) and PMMA A2 (80 nm) were successively spin coated on a SiO$_2$ substrate. Next, bottom bars (270 nm $\times$ 320 nm), 4 global alignment marks (100 µm $\times$ 10 µm) and 4 chief alignment marks (25 µm $\times$ 2 µm) were lithographed with EBL (JEOL 8100) at an acceleration voltage of 100 kV. After exposure, the samples were developed in the solution with a 3:1 mixture of isopropanol (IPA) and methyl isobutyl ketone (MIBK). 3 nm - thick Cr and 30 nm – thick Au layers were subsequently deposited using electron-beam evaporation. After standard lift-off process, SiO$_2$ with a desired thickness was deposited on the first metal array as a dielectric interlayer by magnetron sputtering. The top layer was fabricated using the same method but including a precise alignment process, where the gold alignment marks are applied to ensure the accurate stacking of the top layer. Finally, the reference area near the samples was prepared with a more alignment by direct writer, followed by depositing 5 nm – thick Cr and 150 nm – thick Au layers with magnetron sputtering and performing lift-off process. The top-view pictures of fabricated samples were obtained using SEM (Zeiss Sigma). Note that the bumps in Figs. 4c and 5d are SiO$_2$ bumps stemming from the deposition process

corresponding to the location of the bottom Au bars. The side-view images of the samples were obtained using a dual-beam FIB-SEM which can simultaneously obtain the local sectioning (with the FIB) and imaging (with SEM) of the samples. All samples have lateral dimensions of $100\,\mu m \times 100\,\mu m$.

Optical characterizations

We used a homemade NIR microimaging system equipped with a broadband supercontinuum white light source (Fianium SC400), polarizers, a beam splitter, a CCD, a fiber-coupled grating spectrometer (Ideaoptics NIR2500) and a Princeton Instruments HRS-300 spectrograph with an InGaAs camera to characterize the optical properties of the fabricated samples.

Abbreviations

NF	Near-field
FF	Far-field
EM	Electromagnetic
CMT	Coupled-mode-theory
SI	Supplementary Information
MIM	Metal/insulator/metal
FEM	Finite-element-method
EBL	Electron-beam lithography
LEM	Leaky-eigen-mode
SEM	Scanning-electron-microscopy
FIB	Focus-Ion-Beam
IPA	Isopropanol
MIBK	Methyl isobutyl ketone

Supplementary Information

The online version contains supplementary material available at https://doi.org/10.1186/s43074-022-00078-w.

Additional file 1.

Availability of data and materials

The datasets and figures used and analyzed during the current study are available from the corresponding author on reasonable request.

Declarations

Ethics approval and consent to participate

Not applicable.

Consent for publication

Not applicable.

Competing interests

The authors declare no conflict of interest.

References

1. Schurig D, Mock JJ, Justice BJ, Cummer SA, Pendry JB, Starr AF, et al. Metamaterial electromagnetic cloak at microwave frequencies. Science. 2006;314(5801):977–80. https://doi.org/10.1126/science.1133628.
2. Ni X, Wong ZJ, Mrejen M, Wang Y, Zhang X. An ultrathin invisibility skin cloak for visible light. Science. 2015;349(6254):1310–4. https://doi.org/10.1126/science.aac9411.
3. Jahani Y, Arvelo ER, Yesilkoy F, Koshelev K, Cianciaruso C, De Palma M, et al. Imaging-based spectrometer-less optofluidic biosensors based on dielectric metasurfaces for detecting extracellular vesicles. Nat Commun. 2021;12(1):3246. https://doi.org/10.1038/s41467-021-23257-y.
4. Park J-H, Ndao A, Cai W, Hsu L, Kodigala A, Lepetit T, et al. Symmetry-breaking-induced plasmonic exceptional points and nanoscale sensing. Nat Phys. 2020;16(4):462–8. https://doi.org/10.1038/s41567-020-0796-x.
5. Landy NI, Sajuyigbe S, Mock JJ, Smith DR, Padilla WJ. Perfect metamaterial absorber. Phys Rev Lett. 2008;100(20):207402. https://doi.org/10.1103/PhysRevLett.100.207402.
6. Tian J, Luo H, Li Q, Pei X, Du K, Qiu M. Near-infrared super-absorbing all-dielectric metasurface based on single-layer germanium nanostructures. Laser Photonics Rev. 2018;12(9):1800076. https://doi.org/10.1002/lpor.201800076.
7. Yu N, Genevet P, Kats MA, Aieta F, Tetienne J-P, Capasso F, et al. Light propagation with phase discontinuities: generalized laws of reflection and refraction. Science. 2011;334(6054):333–7. https://doi.org/10.1126/science.1210713.
8. Sun S, He Q, Xiao S, Xu Q, Li X, Zhou L. Gradient-index meta-surfaces as a bridge linking propagating waves and surface waves. Nat Mater. 2012;11(5):426–31. https://doi.org/10.1038/nmat3292.
9. Ni X, Emani NK, Kildishev AV, Boltasseva A, Shalaev VM. Broadband light bending with plasmonic nanoantennas. Science. 2012;335(6067):427. https://doi.org/10.1126/science.1214686.
10. Genevet P, Capasso F, Aieta F, Khorasaninejad M, Devlin R. Recent advances in planar optics: from plasmonic to dielectric metasurfaces. Optica. 2017;4(1):139–52. https://doi.org/10.1364/OPTICA.4.000139.
11. Sun S, He Q, Hao J, Xiao S, Zhou L. Electromagnetic metasurfaces: physics and applications. Adv Opt Photonics. 2019;11(2):380–479. https://doi.org/10.1364/AOP.11.000380.
12. Liu N, Mesch M, Weiss T, Hentschel M, Giessen H. Infrared perfect absorber and its application as plasmonic sensor. Nano Lett. 2010;10(7):2342–8. https://doi.org/10.1021/nl9041033.
13. Qu C, Ma S, Hao J, Qiu M, Li X, Xiao S, et al. Tailor the functionalities of metasurfaces based on a complete phase diagram. Phys Rev Lett. 2015;115(23):235503. https://doi.org/10.1103/PhysRevLett.115.235503.
14. Tian J, Li Q, Belov PA, Sinha RK, Qian W, Qiu M. High-q all-dielectric metasurface: super and suppressed optical absorption. ACS Photonics. 2020;7(6):1436–43. https://doi.org/10.1021/acsphotonics.0c00003.
15. Li Y, Lin J, Guo H, Sun W, Xiao S, Zhou L. A tunable metasurface with switchable functionalities: from perfect transparency to perfect absorption. Adv Opt Mater. 2020;8(6):1901548. https://doi.org/10.1002/adom.201901548.
16. Liang Y, Lin H, Koshelev K, Zhang F, Yang Y, Wu J, et al. Full-stokes polarization perfect absorption with diatomic metasurfaces. Nano Lett. 2021;21(2):1090–5. https://doi.org/10.1021/acs.nanolett.0c04456.
17. Zhang S, Genov DA, Wang Y, Liu M, Zhang X. Plasmon-induced transparency in metamaterials. Phys Rev Lett. 2008;101(4):047401. https://doi.org/10.1103/PhysRevLett.101.047401.
18. Liu N, Langguth L, Weiss T, Kästel J, Fleischhauer M, Pfau T, et al. Plasmonic analogue of electromagnetically induced transparency at the drude damping limit. Nat Mater. 2009;8(9):758–62. https://doi.org/10.1038/nmat2495.
19. Gu J, Singh R, Liu X, Zhang X, Ma Y, Zhang S, et al. Active control of electromagnetically induced transparency analogue in terahertz metamaterials. Nat Commun. 2012;3(1):1151. https://doi.org/10.1038/ncomms2153.
20. Yang Y, Kravchenko II, Briggs DP, Valentine J. All-dielectric metasurface analogue of electromagnetically induced transparency. Nat Commun. 2014;5(1):5753. https://doi.org/10.1038/ncomms6753.
21. Wang C, Jiang X, Zhao G, Zhang M, Hsu CW, Peng B, et al. Electromagnetically induced transparency at a chiral exceptional point. Nat Phys. 2020;16(3):334–40. https://doi.org/10.1038/s41567-019-0746-7.
22. Khorasaninejad M, Chen WT, Devlin RC, Oh J, Zhu AY, Capasso F. Metalenses at visible wavelengths: diffraction-limited focusing and subwavelength resolution imaging. Science. 2016;352(6290):1190–4. https://doi.org/10.1126/science.aaf6644.
23. Zhang F, Pu M, Li X, Gao P, Ma X, Luo J, et al. All-dielectric metasurfaces for simultaneous giant circular asymmetric transmission and wavefront shaping based on asymmetric photonic spin-orbit interactions. Adv Funct Mater. 2017;27(47):1704295. https://doi.org/10.1002/adfm.201704295.
24. Lou Y, Fang Y, Ruan Z. Optical computation of divergence operation for vector fields. Phys Rev Appl. 2020;14(3):034013. https://doi.org/10.1103/PhysRevApplied.14.034013.
25. Lee N, Kim R, Kim JY, Ko JB, Park S-HK, Kim SO, et al. Self-assembled nano–lotus pod metasurface for light trapping. ACS Photonics. 2021;8(6):1616–22. https://doi.org/10.1021/acsphotonics.0c01882.
26. Kim M, Lee D, Yang Y, Kim Y, Rho J. Reaching the highest efficiency of spin hall effect of light in the near-infrared using all-dielectric metasurfaces. Nat Commun. 2022;13(1):2036. https://doi.org/10.1038/s41467-022-29771-x.
27. Meng C, Thrane PCV, Ding F, Bozhevolnyi SI. Full-range birefringence control with piezoelectric mems-based metasurfaces. Nat Commun. 2022;13(1):2071. https://doi.org/10.1038/s41467-022-29798-0.
28. Ma Q, Liu C, Xiao Q, Gu Z, Gao X, Li L, et al. Information metasurfaces and intelligent metasurfaces. Photonics Insights. 2022;1(1):R01. https://doi.org/10.3788/pi.2022.r01.
29. Chen H-T, Zhou J, O'Hara JF, Chen F, Azad AK, Taylor AJ. Antireflection coating using metamaterials and identification of its mechanism. Phys Rev Lett. 2010;105(7):073901. https://doi.org/10.1103/PhysRevLett.105.073901.
30. Chu H, Zhang H, Zhang Y, Peng R, Wang M, Hao Y, et al. Invisible surfaces enabled by the coalescence of anti-reflection and wavefront controllability in ultrathin metasurfaces. Nat Commun. 2021;12(1):4523. https://doi.org/10.1038/s41467-021-24763-9.

31. Lavigne G, Caloz C. Generalized Brewster effect using bianisotropic metasurfaces. Opt Express. 2021;29(7):11361–70. https://doi.org/10.1364/oe.423078.

32. Luo J, Chu H, Peng R, Wang M, Li J, Lai Y. Ultra-broadband reflectionless Brewster absorber protected by reciprocity. Light-Sci Appl. 2021;10(1):89. https://doi.org/10.1038/s41377-021-00529-2.

33. Chu H, Xiong X, Gao Y-J, Luo J, Jing H, Li C-Y, et al. Diffuse reflection and reciprocity-protected transmission via a random-flip metasurface. Sci Adv. 2021;7(37):eabj0935. https://doi.org/10.1126/sciadv.abj0935.

34. Epstein A, Wong JPS, Eleftheriades GV. Cavity-excited huygens' metasurface antennas for near-unity aperture illumination efficiency from arbitrarily large apertures. Nat Commun. 2016;7(1):10360. https://doi.org/10.1038/ncomms10360.

35. Chen K, Feng Y, Monticone F, Zhao J, Zhu B, Jiang T, et al. A reconfigurable active huygens' metalens. Adv Mater. 2017;29(17):1606422. https://doi.org/10.1002/adma.201606422.

36. Liu M, Choi D-Y. Extreme huygens' metasurfaces based on quasi-bound states in the continuum. Nano Lett. 2018;18(12):8062–9. https://doi.org/10.1021/acs.nanolett.8b04774.

37. Liu M, Powell DA, Zarate Y, Shadrivov IV. Huygens' metadevices for parametric waves. Phys Rev X. 2018;8(3):031077. https://doi.org/10.1103/PhysRevX.8.031077.

38. Pfeiffer C, Grbic A. Metamaterial huygens' surfaces: tailoring wave fronts with reflectionless sheets. Phys Rev Lett. 2013;110(19):197401. https://doi.org/10.1103/PhysRevLett.110.197401.

39. Pfeiffer C, Emani NK, Shaltout AM, Boltasseva A, Shalaev VM, Grbic A. Efficient light bending with isotropic metamaterial huygens' surfaces. Nano Lett. 2014;14(5):2491–7. https://doi.org/10.1021/nl5001746.

40. Yu YF, Zhu AY, Paniagua-Domínguez R, Fu YH, Luk'yanchuk B, Kuznetsov AI. High-transmission dielectric metasurface with 2π phase control at visible wavelengths. Laser Photonics Rev. 2015;9(4):412–8. https://doi.org/10.1002/lpor.201500041.

41. Fan K, Suen JY, Liu X, Padilla WJ. All-dielectric metasurface absorbers for uncooled terahertz imaging. Optica. 2017;4(6):601. https://doi.org/10.1364/OPTICA.4.000601.

42. Asadchy VS, Faniayeu IA, Ra'di Y, Khakhomov SA, Semchenko IV, Tretyakov SA. Broadband reflectionless metasheets: frequency-selective transmission and perfect absorption. Phys Rev X. 2015;5(3):031005. https://doi.org/10.1103/PhysRevX.5.031005.

43. Zhou H, Zhen B, Hsu CW, Miller OD, Johnson SG, Joannopoulos JD, et al. Perfect single-sided radiation and absorption without mirrors. Optica. 2016;3(10):1079. https://doi.org/10.1364/OPTICA.3.001079.

44. Londoño M, Sayanskiy A, Araque-Quijano JL, Glybovski SB, Baena JD. Broadband huygens' metasurface based on hybrid resonances. Phys Rev Appl. 2018;10(3):034026. https://doi.org/10.1103/PhysRevApplied.10.034026.

45. Feng T, Potapov AA, Liang Z, Xu Y. Huygens metasurfaces based on congener dipole excitations. Phys Rev Appl. 2020;13(2):021002. https://doi.org/10.1103/PhysRevApplied.13.021002.

46. Prodan E, Radloff C, Halas NJ, Nordlander P. A hybridization model for the plasmon response of complex nanostructures. Science. 2003;302(5644):419–22. https://doi.org/10.1126/science.1089171.

47. Fan JA, Wu C, Bao K, Bao J, Bardhan R, Halas NJ, et al. Self-assembled plasmonic nanoparticle clusters. Science. 2010;328(5982):1135–8. https://doi.org/10.1126/science.1187949.

48. Zhang S, Ye Z, Wang Y, Park Y, Bartal G, Mrejen M, et al. Anti-hermitian plasmon coupling of an array of gold thin-film antennas for controlling light at the nanoscale. Phys Rev Lett. 2012;109(19):193902. https://doi.org/10.1103/PhysRevLett.109.193902.

49. Lin J, Qiu M, Zhang X, Guo H, Cai Q, Xiao S, et al. Tailoring the lineshapes of coupled plasmonic systems based on a theory derived from first principles. Light-Sci Appl. 2020;9(1):158. https://doi.org/10.1038/s41377-020-00386-5.

50. Fan S, Suh W, Joannopoulos JD. Temporal coupled-mode theory for the Fano resonance in optical resonators. J Opt Soc Am A. 2003;20(3):569–72. https://doi.org/10.1364/JOSAA.20.000569.

51. Suh W, Wang Z, Fan S. Temporal coupled-mode theory and the presence of non-orthogonal modes in lossless multimode cavities. IEEE J Quantum Electron. 2004;40(10):1511–8. https://doi.org/10.1109/JQE.2004.834773.

52. Hsu CW, Zhen B, Lee J, Chua S-L, Johnson SG, Joannopoulos JD, et al. Observation of trapped light within the radiation continuum. Nature. 2013;499(7457):188–91. https://doi.org/10.1038/nature12289.

53. We choose to design/characterize our resonator #2 with h set as the optimized value yielding the achromatic reflectionless bi-layer metasurface. While optical response of such a resonator slightly changes as h varies, we neglect such deviations in the discussions followed.

Publisher's Note

Springer Nature remains neutral with regard to jurisdictional claims in published maps and institutional affiliations.